

# Electron Transport Properties of $\text{Al}_x\text{Ga}_{1-x}\text{N}/\text{GaN}$ Transistors Based on First-Principles Calculations and Boltzmann-Equation Monte Carlo Simulations


Jingtian Fang,<sup>1,2,3,\*</sup> Massimo V. Fischetti,<sup>4</sup> Ronald D. Schrimpf,<sup>2</sup> Robert A. Reed,<sup>2</sup> Enrico Bellotti,<sup>3</sup> and Sokrates T. Pantelides<sup>1,2</sup>

<sup>1</sup>*Department of Physics and Astronomy, Vanderbilt University, Nashville, Tennessee 37235, USA*

<sup>2</sup>*Department of Electrical Engineering and Computer Science, Vanderbilt University, Nashville, Tennessee 37235, USA*

<sup>3</sup>*Department of Electrical and Computer Engineering, Boston University, Boston, Massachusetts 02215, USA*

<sup>4</sup>*Department of Materials Science and Engineering, The University of Texas at Dallas, Richardson, Texas 75080, USA*

 (Received 8 December 2018; revised manuscript received 30 January 2019; published 15 April 2019)

High-electron-mobility transistors (HEMTs) based on  $\text{Al}_x\text{Ga}_{1-x}\text{N}/\text{GaN}$  heterostructures have great potential for applications in power electronics and radio frequency applications. Operating under large bias and electric fields, hot electrons are present in the channel where they can activate preexisting benign defects that cause scattering or carrier trapping, resulting in device degradation, such as threshold-voltage shifts and transconductance degradation. We report a comprehensive investigation of the electron transport properties of wurtzite-phase GaN and AlN and of an  $\text{Al}_{0.25}\text{Ga}_{0.75}\text{N}/\text{GaN}$  HEMT by solving the Boltzmann transport equation with a synchronous ensemble Monte Carlo technique and employing first-principles electronic properties, including the full energy bands, phonon dispersions, and electron-phonon scattering rates. We find that, for electron collisions with the highest-energy optical phonon mode, nonpolar scattering by optical phonons contributes comparable to polar scattering. Polar scattering with acoustic phonons, that is, piezoelectric scattering, is found to be as important as the polar scattering with optical phonons for low-energy electrons at room temperature. We compare the calculated high-field transport characteristics of bulk GaN with previously reported results. We also calculate the nonpolar acoustic deformation potential, nonpolar optical deformation potential, and high-field transport characteristics of bulk AlN. We find that inclusion of piezoelectric scattering results in a low-field electron mobility of approximately  $450 \text{ cm}^2/(\text{V s})$ , which is very close to the experimental value. Simulation results are presented for an  $\text{Al}_{0.25}\text{Ga}_{0.75}\text{N}/\text{GaN}$  HEMT, including electric field, average carrier kinetic energy, and drift velocity in the channel. Finally, we present the carrier energy distribution function in the conducting channel, which is key to accurately determine hot-carrier-caused device degradation and identify possible routes to an improved device design.

DOI: [10.1103/PhysRevApplied.11.044045](https://doi.org/10.1103/PhysRevApplied.11.044045)

## I. INTRODUCTION

Electronic and optoelectronic devices based on wide band-gap semiconductors are very important for power electronics. Among several such materials that have been studied, such as SiC [1], GaN [2–6], diamond [7], and  $\text{Ga}_2\text{O}_3$  [8,9], GaN in the wurtzite structure has attracted much interest thanks to its high breakdown field (as large as 4 MV/cm, compared to 0.3 MV/cm for silicon) and low *on* resistance, properties amenable to applications in smart electrical grids such as a power switch [2]. The high peak velocity ( $2.5 \times 10^7 \text{ cm/s}$ ) and saturation velocity ( $1.3 \times 10^7 \text{ cm/s}$ ) permit fast transit times and high-frequency amplifiers. There are also promising

applications for blue light-emitting diodes [4,5,10] and ultraviolet avalanche photodiodes [11].

High-electron-mobility transistors (HEMTs) based on  $\text{Al}_x\text{Ga}_{1-x}\text{N}/\text{GaN}$  heterostructures in the wurtzite phase, also referred to as “heterostructure field-effect transistors” (HFETs), are widely studied because of the large interfacial two-dimensional (2D) electron gas (2DEG) density (approximately  $1\text{--}2 \times 10^{13} \text{ cm}^{-2}$ , compared with  $10^{12} \text{ cm}^{-2}$  for AlGaAs/GaAs HFETs) without any intentional doping in the channel region [3,6]. Electron mobilities as high as  $10\,000 \text{ cm}^2/(\text{V s})$  at 77 K and approximately  $1300 \text{ cm}^2/(\text{V s})$  at RT have been reported [12]. These properties of high breakdown field, large 2DEG density, and high RT electron mobility lead to high current and high-power output. GaN in the cubic phase is less attractive since it is not thermodynamically stable and has zero

\*jingtian.fang@utdallas.edu

spontaneous polarization. Very recently,  $\text{Al}_x\text{In}_{1-x}\text{N}/\text{GaN}$  heterostructures have also been reported exhibiting a high carrier density of approximately  $2 \times 10^{13} \text{ cm}^{-2}$ , but with a lower RT mobility [13]. The oxide heterostructure  $\gamma\text{-Al}_2\text{O}_3/\text{SrTiO}_3$  has also been shown to exhibit an extremely high sheet carrier density of approximately  $4 \times 10^{14} \text{ cm}^{-2}$  and an electron mobility of about  $140\,000 \text{ cm}^2/(\text{V s})$  at temperatures lower than 5 K [14]. However, the RT mobility is significantly degraded to about  $10 \text{ cm}^2/(\text{V s})$ . The band gap and band offset of  $\text{Ga}_2\text{O}_3$  and  $(\text{Al}_x\text{Ga}_{1-x})_2\text{O}_3$  alloys, which are emerging materials for similar devices, have also been reported recently [9].

Operating under large bias and high electric fields, the performance of  $\text{Al}_x\text{Ga}_{1-x}\text{N}/\text{GaN}$  HEMTs is limited, however, by defects that are activated by the hot carriers that are readily excited in the channel [15–17]. The activated defects lead to charge trapping and thus threshold-voltage shifts and transconductance degradation [18–20]. Therefore, a detailed knowledge of the carrier energy distribution in the conducting channel is essential in order to quantify the activated-defect density and correlate it to the threshold-voltage shifts and transconductance degradation. Device simulation is necessary to understand the device operation and failure mechanisms and to facilitate electronics development. Although quantum transport simulations are necessary for sub-10-nm devices [21,22], for the HEMTs of interest, the established method of choice to treat carrier transport is based on the MC solutions of the Boltzmann transport equation accounting for the electronic band structure [23–26].

Several MC studies of high-field transport in bulk wurtzite-phase GaN [26–33] and AlN [31,34] have been reported previously. Wu *et al.* have calculated the high-field velocity-field characteristics and have used them in drift-diffusion equations to simulate  $\text{Al}_x\text{Ga}_{1-x}\text{N}/\text{GaN}$  HEMTs [28]. However, the electron energy range they can treat correctly is restricted by the limited validity of the nonparabolic three-valley model employed to approximate the band structure. As a result, they have reported an unphysically strong velocity overshoot in the channel [Ref. [35], Fig. 2(a)]. On the contrary, the full electronic band structure used by Moresco *et al.* [11] and Bertazzi *et al.* [26] in their MC simulations of GaN-based avalanche photodetectors allows them to simulate electron transport at larger electric fields, so that even impact ionization can be well described. Moresco *et al.* have shown that using the full band structure, calculated from empirical pseudopotentials, makes it possible to also account for band-to-band tunneling and leads to a considerable increase of the impact ionization coefficients, compared to the case in which band-to-band tunneling is not considered [26]. This accurately reproduces the measured electron and hole multiplication gains for a variety of electron- and hole-injected avalanche photodetectors [11]. It has also been shown by Shichijo *et al.* that it is imperative to account for the full

electronic band structure of the material in order to correctly handle impact ionization in GaAs and Si devices [24]. Fischetti and Laux have shown that in silicon devices, the parabolic-bands approximation, as well as the nonparabolic approximation, overestimates the average carrier kinetic energy, carrier drift velocity, and the peak energy at the drain end of the devices [23].

In addition to employing an accurate treatment of the electronic structure, a reliable study of transistor performance requires a careful analysis of carrier-phonon scattering. For example, it has been shown that for GaN, the intervalley deformation potentials change significantly for transitions away from the valley minima (see Ref. [26], Fig. 3 and Ref. [33], Fig. 8). These important features can be accounted for only when relying on sophisticated models to treat the electron-phonon interaction, for example, by employing the full matrix elements (obtained from *ab initio* calculations) rather than using a constant deformation potential [36]. When calculating the high-field transport characteristics and impact-ionization coefficients of wurtzite GaN, Bertazzi *et al.* used nonlocal empirical pseudopotentials to obtain the electronic band structure and electron-phonon scattering rates [26]. Similarly, in calculating the high-field transport characteristics of GaN, Yamakawa *et al.* have used the rigid-ion model of the electron-phonon interaction, accounting for the anisotropy of transport parameters [33]. These demonstrations motivate the adoption of the full-band MC method for simulating wurtzite-phase  $\text{Al}_x\text{Ga}_{1-x}\text{N}/\text{GaN}$  HEMTs with materials properties calculated from first-principles methods. To our best knowledge, such calculations have not yet been performed or reported. We note that the key contribution of the Density-functional theory (DFT) calculations is to provide first-principles, parameter-free electron-phonon scattering matrix elements in contrast to prior work based on empirical pseudopotential energy bands that employs phenomenological models to describe electron-phonon coupling.

In this work, we calculate the full electronic band structure, phonon dispersion, and electron-phonon scattering rates using first-principles methods. This provides an avenue to perform truly predictive calculations of materials' electronic transport properties. We find that for the electron scattering with the highest-energy optical phonon branches, nonpolar processes give a contribution comparable to polar processes. In the past, this feature has not been observed when using empirical methods. Furthermore, polar scattering with acoustic phonons, that is, piezoelectric scattering, is found to be as important as the polar scattering with optical phonons for low-energy electrons at RT. We compare the high-field transport characteristics of bulk GaN with previously published results. We also present results regarding the nonpolar acoustic deformation potential, the nonpolar optical deformation potential, and the high-field transport characteristics of

bulk AlN, based on material properties calculated from first principles. We find that inclusion of polar scattering with acoustic phonons results in a low-field electron mobility of approximately  $450 \text{ cm}^2/(\text{V s})$ , which is very close to the experimental value. Finally, we show the simulation results for an  $\text{Al}_{0.25}\text{Ga}_{0.75}\text{N}/\text{GaN}$  HEMT, including electric field, the average kinetic energy, and drift velocity of carriers in the channel. Our results show a physical velocity overshoot in the channel compared with previous reports using simpler multivalley MC simulations [Ref. [35], Fig. 2(a)]. The reported simulation results and their agreement with experimental results illustrates the predictivity and physical accuracy of using first-principles band structures and scattering rates for advanced semiconductor device simulation.

The paper is organized as follows. Section II briefly describes the calculation of the electronic band structure, the phonon dispersion, and the electron-phonon scattering rates using first-principles method. Section II also succinctly discusses the full-band MC simulation approach. In Sec. III A, we present the electronic, vibrational, and electron-phonon scattering properties of bulk GaN and in Sec. III B, we present the low-field and high-field transport characteristics. Section III C describes the electronic band structure, phonon dispersion, electron-phonon scattering rate, and low-field and high-field transport characteristics of electrons in bulk AlN. Finally, the simulation of an  $\text{Al}_{0.25}\text{Ga}_{0.75}\text{N}/\text{GaN}$  HEMT is presented in Sec. IV. We conclude the work in Sec. V.

## II. COMPUTATIONAL METHODS

In this work, both the electronic band structure and the phonon dispersion are calculated by using a first-principles density-functional theory computer code, QUANTUM-ESPRESSO [37]. Norm-conserving pseudopotentials

[38] with the local density approximation (LDA) for the exchange-correlation functional are employed. The comparison of the satellite-valley energies with other first-principles calculations, shown below in Table I, and the effective masses at the conduction band minimum and other valley minima, shown below in Table II, indicate that using LDA for the exchange-correlation functional is sufficient to capture the critical electron transport parameters. For the phonon spectra, we calculate the dynamical matrix using density-functional perturbation theory. The electron-phonon scattering rates are calculated using first-principles methods, in particular, the Wannier-function-based scheme implemented in the ‘‘Electron-Phonon coupling using Wannier functions’’ (EPW) program [51–53]. The maximally localized Wannier functions are provided by the WANNIER90 software package [54]. The Wannier-Fourier interpolation technique, a component of EPW, significantly reduces the computational burden of electron-phonon calculations [53].

In order to perform efficient full-band MC simulations, we generate in the first octant of the first Brillouin zone a coarse grid of 3090  $\mathbf{k}$  points with a uniform spacing of  $\Delta k = 0.033 \times 2\pi/a$ ,  $a$  being the lattice constant. At these  $\mathbf{k}$  points, we compute the electron dispersion,  $E_n(\mathbf{k})$ , their first-order derivatives,  $\partial E_n(\mathbf{k})/\partial \mathbf{k}$ , and the second-order derivatives,  $\partial^2 E_n(\mathbf{k})/\partial k_i \partial k_j$  ( $i, j = x, y, z$ ), storing this information in a look-up table. The index  $n$  labels the electronic band. This index runs over the five lowest-energy conduction bands, since these are sufficient to study sub-10-eV electron transport at the largest electric fields applied to the devices. The energies  $E_n(\mathbf{k})$  for an arbitrary wavevector  $\mathbf{k}$  can be obtained by interpolating the energies stored in the coarse mesh, as explained in Ref. [23]. These quantities can be obtained in the other octants of the Brillouin zone through trivial symmetry transformations.

TABLE I. The conduction band energies at different satellite valleys (in unit of eV). The conduction band energy at the  $\Gamma$  valley of the first conduction band is set as the zero reference energy.

		$K$	$U$	$L$	$A$	$\Gamma^3$	$M$
GaN	This work	2.82	1.95	2.23	2.25	2.23	2.84
	LDA + $G_0W_0$ (Ref.[39])	3.06	2.32	2.60	2.43	2.50	3.27
	GW (Ref. [40])	3.1		2.5	2.6	2.4	3.0
	EPM (Ref. [41])	1.59	1.34			2.14	1.87
	EPM (Ref.[42])	3.08		2.43	2.37	2.35	3.05
	Expt. (Ref. [43])			$0.90 \pm 0.08$			
	Expt. (Ref.[44])			$0.97 \pm 0.02$			
	Expt. (Ref.[45])		1.34				
AlN	This work	0.64	0.61	0.92	2.11	2.27	1.33
	LDA + $G_0W_0$ (Ref.[39])	0.84	0.67	0.99	2.28	2.65	1.57
	GW (Ref. [40])	0.9		1.1	2.5	2.5	1.6
	EPM (Ref. [41])	0.9	1.05			2.49	1.68
	EPM (Ref. [42])	1.26		1.32	2.33	2.46	1.95

EPM, empirical pseudopotentials method; LDA, local density approximation.

TABLE II. Electron effective mass (in units of free electron mass  $m_0$ ) along different crystalline directions at different valleys of the first conduction band and acoustic phonons' sound velocities of GaN

	This work	Other work
$m_{\Gamma}^*$ ( $\Gamma \rightarrow K$ )	0.20	0.18 <sup>a</sup> , 0.36 <sup>b</sup>
$m_K^*$ ( $K \rightarrow \Gamma$ )	0.64	0.47 <sup>c</sup>
$m_K^*$ ( $K \rightarrow M$ )	0.65	
$m_M^*$ ( $M \rightarrow K$ )	0.21	0.565 <sup>c</sup>
$m_M^*$ ( $M \rightarrow \Gamma$ )	4.18	
$m_{\Gamma}^*$ ( $\Gamma \rightarrow M$ )	0.20	0.18 <sup>a</sup> , 0.33 <sup>b</sup> , 0.2 <sup>c</sup> , 0.20 <sup>d</sup> , 0.21 <sup>e</sup> , 0.2283 <sup>f</sup> , 0.20 <sup>g</sup> , 0.23 <sup>h</sup>
$m_{\Gamma}^*$ ( $\Gamma \rightarrow A$ )	0.18	0.20 <sup>a</sup> , 0.27 <sup>b</sup> , 0.1846 <sup>f</sup> , 0.19 <sup>h</sup>
$m_A^*$ ( $A \rightarrow \Gamma$ )	-0.54	
$m_A^*$ ( $A \rightarrow H$ )	0.37	
$m_U^*$ ( $U \rightarrow L/M$ )	0.33	0.442 <sup>c</sup> , 0.285 <sup>d</sup> , 0.25 <sup>e</sup>
$m_L^*$ ( $L \rightarrow H$ )	0.32	
$m_L^*$ ( $L \rightarrow A$ )	1.02	
$m_A^*$ ( $A \rightarrow L$ )	0.37	
$c_s^{LA}$ ( $\Gamma \rightarrow A$ )	7930	7641 <sup>e</sup> , 6600 <sup>i</sup>
$c_s^{TA}$ ( $\Gamma \rightarrow A$ )	3994	4110 <sup>e</sup> , 2700 <sup>i</sup>

<sup>a</sup>Ref. [46], LDA.

<sup>b</sup>Ref. [47], LCAO: linear combination of atomic orbitals.

<sup>c</sup>Ref. [41], EPM.

<sup>d</sup>Ref. [50].

<sup>e</sup>Ref. [20].

<sup>f</sup>Ref. [42], EPM.

<sup>g</sup>Ref. [48], Expt.

<sup>h</sup>Ref. [49], LMTO: linear muffin-tin orbital.

<sup>i</sup>Ref. [30].

We also calculate the electron scattering rates with all phonon branches, including phonon emission and absorption, at the given 3090  $\mathbf{k}$  points. As both GaN and AlN in their wurtzite structure are polar materials, we calculate both the total scattering rate and the polar contribution to the total electron scattering rate with each phonon mode. The nonpolar contribution can then be determined as well. The polar contribution of the electron scattering process with each phonon mode is determined by considering only the long-range interaction, as described in Ref. [51]. Note that we use a fine  $\mathbf{q}$  mesh of  $40 \times 40 \times 40$  points and obtain a reasonable convergence of the scattering rates from the first-principles calculations. Giustino *et al.* probe the accuracy limit of *ab initio* calculations of the carrier mobility in silicon within the framework of the Boltzmann transport equation. They have shown that fully predictive calculations of the electron and hole mobilities require an extremely fine sampling around the valley minima [55].

We simulate electron transport properties using the methods described in Refs. [23,25] by solving the Boltzmann transport equation with the calculated band

structure, phonon dispersion, and electron-phonon scattering rates. For convenience and efficiency of selecting the scattering processes when solving the Boltzmann transport equation—and also to account for the difference of the angular dependence of different scattering processes—we group the electron-phonon scattering into four categories. The first two groups consist of nonpolar and polar scattering processes with acoustic phonons, respectively. The third group includes nonpolar processes with optical phonons. Finally, the last group includes the polar component of the electron scattering with the optical modes. After a summation of the electron scattering rates with all the phonon branches in the respective groups, we store them in another look-up table. For the selection of the final states after a collision, we assume coupling constants with a  $q$  dependence for nonpolar acoustic scattering processes, independent of  $q$  for nonpolar optical scattering processes, and  $1/q$  dependence for the polar scattering processes [23].

### III. BULK MATERIALS' PROPERTIES FROM FIRST-PRINCIPLES CALCULATIONS

#### A. GaN first-principles transport properties

For wurtzite GaN, we use the experimentally measured lattice constants  $a = 3.215$  Å and  $c = 5.241$  Å [56] and no further relaxation is performed. The valley energies and the valley effective masses we show below in Tables I and II justify the appropriateness of this choice of using the experimental lattice constants. Two Ga atoms and two N atoms are present in the primitive cell. Their respective atomic positions represented in the basis of real space primitive translation vectors are  $(2/3, 1/3, 0)$ ,  $(1/3, 2/3, 0.5)$ ,  $(2/3, 1/3, 0.376)$ , and  $(1/3, 2/3, 0.876)$ .

Figure 1(a) shows the electronic band structure of wurtzite GaN along certain high-symmetry lines. We only show the lowest five conduction bands dispersions since we restrict the study of this work to electron transport. The lowest five conduction bands permit the simulation of carrier transport up to kinetic energies as high as 9 eV. The calculated band gap is 1.78 eV, smaller than the experimental RT band gap of 3.4 eV. This underestimation of the band gaps for semiconductors and insulators by DFT calculations is commonly known. We apply a scissors operator and rigidly shift up the conduction bands 1.62 eV with respect to the valence bands and obtain a band gap of 3.4 eV.

The energies of the satellite valleys are listed in Table I and compared with previous results [39–45]. The  $U$  valley, which is approximately  $0.28 \times \pi/c$  far away from the  $L$  valley along the high-symmetry line  $LM$ , lies 1.95 eV above the conduction band minimum of the  $\Gamma$  valley. The  $L$  valley,  $A$  valley, and the  $\Gamma$  valley of the second conduction band have similar energies of 2.23 eV above the conduction band minimum. The  $K$  valley of the first conduction

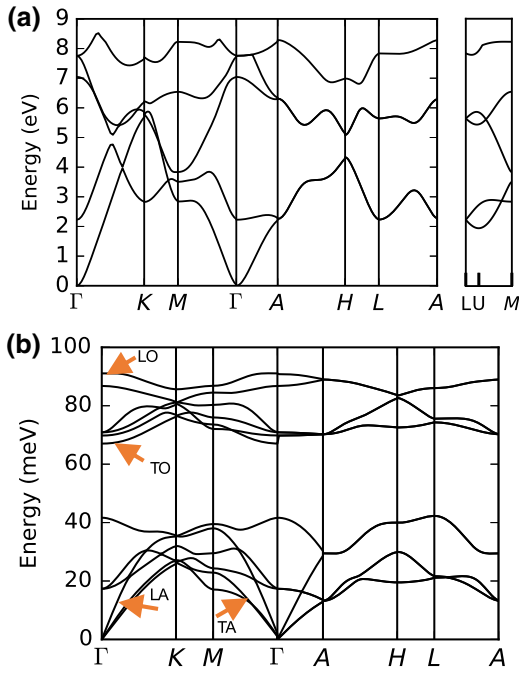


FIG. 1. (a) The energy dispersion of the first five conduction bands along several high-symmetry lines. The conduction band minimum at the  $\Gamma$  valley is set to zero. (b) Full phonon dispersion along several high-symmetry lines of wurtzite GaN. The longitudinal and transverse acoustic phonon branches and the long-range transverse and longitudinal optical phonon branches are all annotated with arrows.

band is 2.82 eV above the conduction band minimum. It is worth mentioning that the three types of valleys employed in simulations by Wu *et al.* are the  $\Gamma^1$  valley,  $\Gamma^3$  valley, and the  $U$  valley [35]. However, from Table I, we can observe that the energies of the  $L$  valleys,  $A$  valleys, and  $\Gamma^3$  valley are all very close. Indeed, if we observe the second conduction band along the high-symmetry line from  $\Gamma$  to  $A$  in Fig. 1(a), the band is nearly dispersionless and electrons with an energy around 2.23 eV can be distributed equally along this path, as demonstrated in Sec. II B.

There exists a controversy regarding the energy separation of the  $\Gamma^1$  valley and  $L$  valley. Recent experiments have suggested a value of approximately 0.8 to 1 eV [43,44,57], much smaller than those predicted by *ab initio* calculations of about 2.1–2.2 eV [39,40,47]. However, questions have been raised about the validity of these measurements [58] and most of the MC results reported previously have been obtained using the theoretical value of approximately 2.2 eV predicted by the *ab initio* calculations [39,40,47]. Therefore, here, we also employ this larger value.

The effective masses extracted from the band structure in the first-conduction-band valleys are listed in Table II. The effective mass of the  $\Gamma$  valley for the first conduction band is  $0.2 m_0$  (where  $m_0$  is the free electron mass), which is the same as the experimental value reported by Drechsler

*et al.* [48] and is also very close to the experimental value reported by Witowski,  $0.222 m_0$  [59]. The effective mass obtained for the  $\Gamma$  valley of the second conduction band is  $0.28 m_0$ , which is quite different from that assumed by the multivalley MC simulations [30,60]. Chen *et al.* used the free electron mass without any suitable calibration [60] and Bhapkar *et al.* used  $0.6 m_0$ , which is determined from digitizing the band dispersion reported in Ref. [30].

Figure 1(b) shows the phonon dispersion of all twelve phonon branches along several high-symmetry lines. The highest-energy optical phonon branches have a maximum energy of 91.2 meV at the  $\Gamma$  point. This phonon dispersion is close to that calculated using a phenomenological model [61] and to that based on *ab initio* calculations [62]. The discontinuities at the  $\Gamma$  point in the optical-phonon energies along the  $M$ - $\Gamma$  and  $\Gamma$ - $A$  directions are due to the anisotropic nature of the wurtzite structure and to the fact that these optical modes have an angular dependence [62]. The sound velocities of the longitudinal acoustic phonon and the transverse acoustic phonon extracted from the phonon dispersion are 7930 and 3994 m/s, respectively [63], as listed in Table II.

We first compare the polar scattering contribution and the nonpolar scattering contribution for two electronic states scattering with all 12 phonon branches in Figs. 2(a) and 2(b). We find that the polar contribution is minimal for electron scattering with the eight lower-energy optical phonon branches. Therefore, we consider these electron-phonon processes as fully nonpolar. For electron scattering with the highest-energy optical phonon branch instead, the polar contribution and the nonpolar contribution are comparable. We show the calculated polar and nonpolar scattering with optical phonons in Fig. 2(c) and the polar and nonpolar scattering with acoustic phonons in Fig. 2(d). It can be observed that the polar scattering rate with acoustic phonons is very similar to the polar scattering with optical phonons at low energies and plays an important role in determining the low-field electron mobility at RT as well.

We also show in Figs. 2(c) and 2(d) the scattering rates calculated with an analytical formula to fit the first-principles scattering rates [25]. For the nonpolar scattering rates with acoustic phonons, we use an effective mass of  $0.2 m_0$ , a nonparabolicity factor of  $0.58 \text{ eV}^{-1}$ , and an intravalley deformation potential in the  $\Gamma$  valley of approximately 4.0 eV. Note that the nonparabolicity factor,  $\alpha$ , is defined as  $\gamma(\mathbf{k}) = E_n(\mathbf{k}) \cdot [1 + \alpha \cdot E_n(\mathbf{k})]$  where  $\gamma(\mathbf{k}) = \hbar^2 \mathbf{k}^2 / 2m^*$ . For the nonpolar scattering rates with optical phonons, we use an optical deformation potential of  $3.8 \times 10^8 \text{ eV/cm}$ . We also use the conventional Fröhlich expression [64] to calculate the polar coupling constant with the longitudinal optical phonon (LO), using a static relative dielectric constant of 8.9 and a high-frequency relative dielectric constant of 5.35 [65]. Note that Lee *et al.* [66] have concluded that the Fröhlich model [64], which

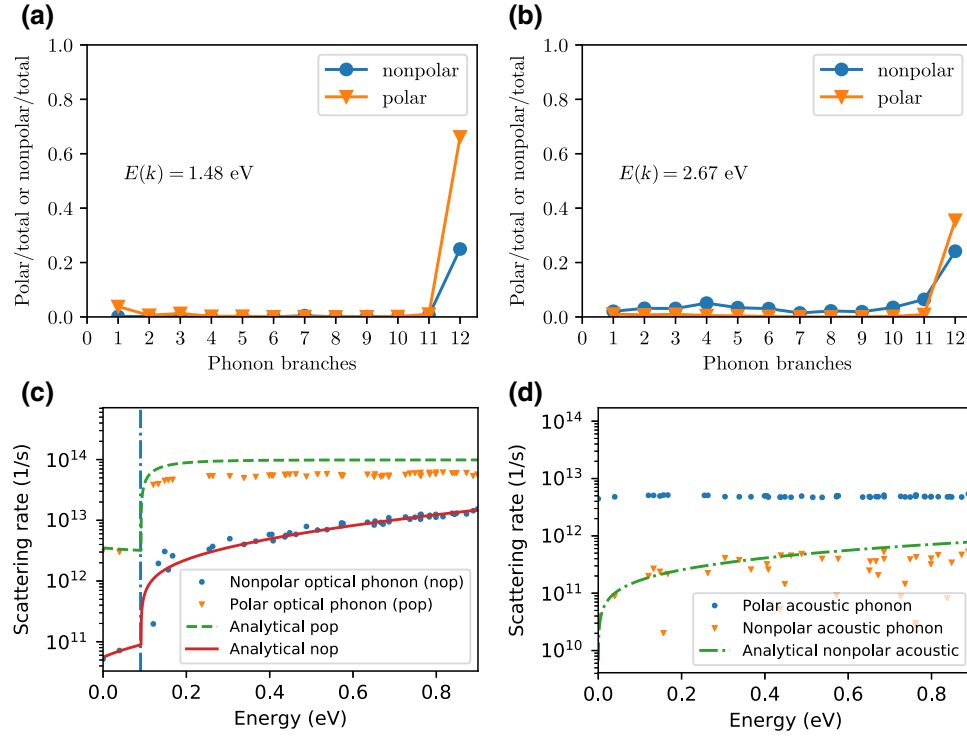


FIG. 2. (a),(b) The ratio of the polar scattering rates to the total scattering rates and the ratio of the nonpolar scattering rates to the total scattering rates with each phonon branch. The total scattering rates are the sum of the rates for collisions with all the 12 phonon branches, including polar and nonpolar processes. Two electronic energy states,  $E_1(k) = 1.48$  eV and  $E_2(k) = 2.67$  eV, are selected for the demonstration. (c) The calculated first-principles polar and nonpolar scattering rates with optical phonons. The vertical dot-dashed line is drawn at the energy of the highest-energy optical phonon mode and is plotted for eye guiding, serving as a separation between low and high energy carriers. (d) The calculated first-principles polar and nonpolar scattering rates with acoustic phonons. The scattering rates calculated using analytical formula are also shown in (c) and (d). The fitting parameters are given in the text.

is applicable to the simple isotropic (i.e., cubic) systems, can be used in wurtzite crystals to describe the electron scattering with the LO phonons.

### B. Low-field and high-field transport properties of GaN

Whereas, in principle, we could have employed the full phonon dispersion for the following full-band MC simulations, for numerical simplicity and computational efficiency, we embrace simplifying approximations. For electron scattering with the acoustic phonon branches, since scattering with the longitudinal acoustic phonon dominates, we assume the electron energy loss following the longitudinal acoustic phonon dispersion relationship

$$\hbar\omega = \begin{cases} \hbar\omega_{\max}[1 - \cos(qa/4)]^{1/2}, & q < 2\pi/a \\ \hbar\omega_{\max}, & q \geq 2\pi/a \end{cases}, \quad (1)$$

where  $q$  is the phonon momentum and  $\omega_{\max} = 4c_{LA}/a$  and  $c_{LA}$  is the longitudinal acoustic phonon sound velocity. For each optical phonon emission, an electron energy loss of 91.2 meV is assumed, corresponding to the energy of the

highest optical phonon mode at the  $\Gamma$  valley. The electron energy gain is the opposite if the scattering results in phonon absorption.

Employing the first-principles band structure and electron-phonon scattering rates, the low-field and high-field transport characteristics of bulk wurtzite GaN along the  $\Gamma$ - $K$  symmetry line in the basal plane are calculated and shown in Fig. 3. Comparison with previous work is illustrated. From our full-band MC simulations, the peak velocity is calculated to be about  $2.8 \times 10^7$  cm/s. Wu *et al.* have calculated the characteristics using the multivalley ensemble MC simulations [28]. Bertazzi *et al.* have reported a peak electron drift velocity of  $2.8 \times 10^7$  cm/s along the  $\Gamma$ - $M$  direction with similar full-band MC techniques [26]. Yamakawa *et al.* have reported a similar peak velocity of  $2.5 \times 10^7$  cm/s calculated by full-band cellular MC model [32]. Albrecht *et al.* employed both a five-valley and a full-band ensemble MC technique to calculate the velocity-field curve [31]. Figure 3 shows their full-band ensemble MC results for comparison. The experimental results from Barker *et al.* are also shown [29]. It has been reported that minor differences can be observed in the drift velocity characteristics when the electric field is applied

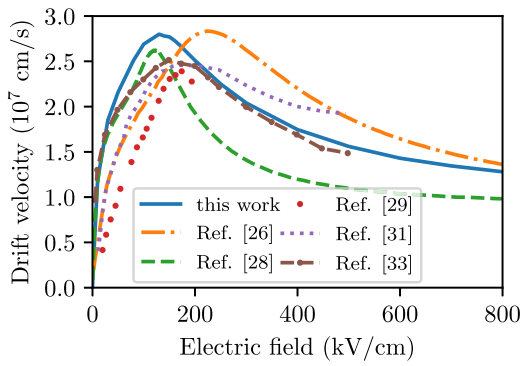


FIG. 3. The steady-state high-field transport characteristics of electrons in GaN when the electric field is applied along the  $\Gamma \rightarrow K$  high-symmetry line in the basal plane. MC simulation results and experimental results from other articles are shown as well for comparison.

along different crystal orientations [31–33]. From the low-field drift velocity characteristics, we extract the phonon-limited mobility of approximately  $1950 \text{ cm}^2/(\text{V s})$ . Vitanov reported a mobility of  $1850 \text{ cm}^2/(\text{V s})$  when piezoelectric scattering is ignored and a mobility of approximately  $1600 \text{ cm}^2/(\text{V s})$  when piezoelectric scattering is considered [20]. These values are in reasonable agreement with the experimental value of approximately  $1300 \text{ cm}^2/(\text{V s})$  [12], considering that the effects of impurity scattering and dislocation scattering are not taken into account in this work.

The difference shown by different MC simulation results arises either from different band structures or from the inclusion of different scattering mechanisms. Compared with the experimental results reported by Barker *et al.* [29], the larger drift velocities reported by all the MC simulations [26,28,31,33] at the low electric fields are either due to the neglect of scattering with defects (such as dislocations and ionized impurities) or due to the neglect of piezoelectric scattering. Note that the results obtained by Wu *et al.* show a fast reduction of the drift velocity at high electric fields, while all other full-band MC simulations show a slower drift velocity drop. The saturation velocity (approximately  $1.3 \times 10^7 \text{ cm/s}$ ) calculated using full-band MC simulations is generally larger than the results obtained by Wu *et al.* This may result in different electron transport properties of  $\text{Al}_x\text{Ga}_{1-x}\text{N}/\text{GaN}$  HEMTs operating at high electric fields.

The distribution of MC particles occupying the first and the second conduction bands in the first Brillouin zone is shown in Fig. 4 for a given electric field strength of  $800 \text{ kV/cm}$ . For particles occupying the first conduction band, most of the particles are located around the  $\Gamma$  valley with momenta exhibiting a noticeable drift along the direction of the applied electric field, with a few particles located around the 12 satellite  $U$  valleys. For particles

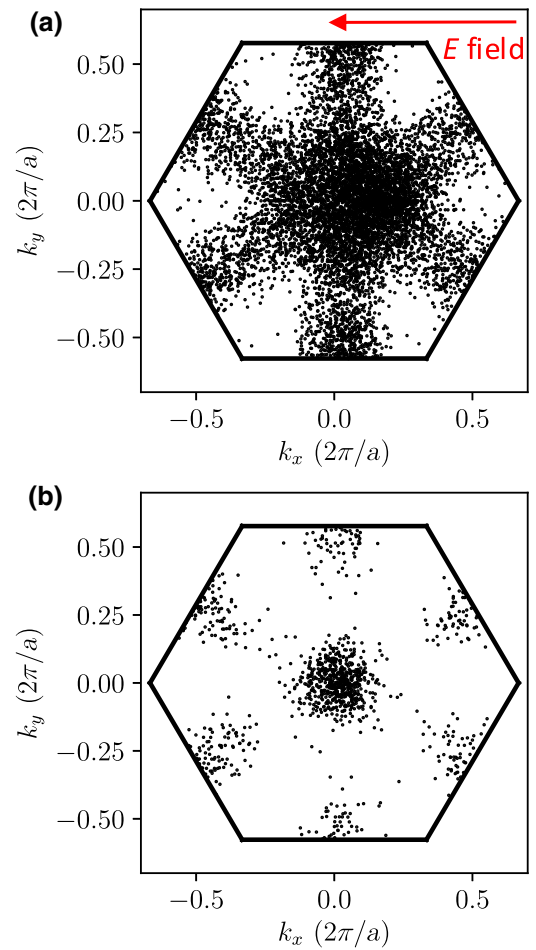


FIG. 4. In GaN, the distribution of MC particles occupying the first conduction band (a) and the second conduction band (b) shown in reciprocal space for an electric field strength of  $800 \text{ kV/cm}$ .

occupying the second conduction band, most particles are distributed along the  $\Gamma$ - $A$  symmetry line. Some particles also occupy the  $L$  valleys. The particle occupation of the valleys is consistent with their energy splitting from the conduction band minimum. A two-dimensional plot in the  $(k_x-k_y)$  basal plane is given for convenience. The average electron energies at different strengths of the electric field are shown in Fig. 5. For electric fields smaller than  $150 \text{ kV/cm}$ , the average electron energies are close to the thermal energy. Above  $150 \text{ kV/cm}$ , the average electron energy increases sharply and then increases slowly again when the field strength exceeds  $500 \text{ kV/cm}$ . The evolution of the particle valley occupancy is the underlying reason for the trend. The trend shown here is similar to the results from the multivalley MC simulation results [30,60].

### C. Electron transport properties of AlN

The experimental lattice constants of wurtzite AlN are  $a = 3.110 \text{ \AA}$  and  $c = 4.980 \text{ \AA}$  [65]. The same coordinates

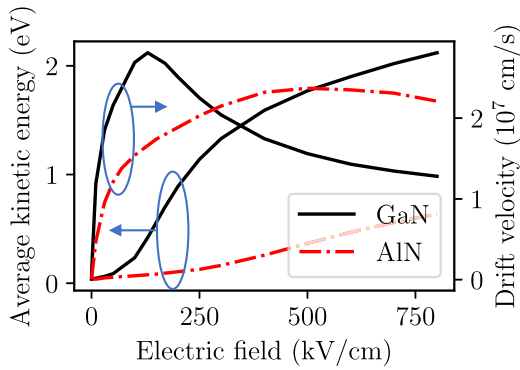


FIG. 5. Characteristics of the electric field vs average electron kinetic energy (left axis) and vs drift velocity (right axis) for GaN and AlN along the  $\Gamma \rightarrow K$  high-symmetry line in the basal plane. The data for GaN are plotted with solid black lines and the data for AlN are plotted with dot-dashed red lines.

in the basis of AlN's real-space primitive translation vectors as those of GaN are used for the atoms in its primitive cell. The band structure is shown in Fig. 6(a). The conduction band energies of several satellite valleys are listed in Table I. Measured from the lowest conduction band at the  $\Gamma$  valley minima,  $E_0 = 0$ , the  $K$  valleys in the first band are 0.64 eV above  $E_0$ . The energy of the  $U$  valleys in the first band, which are located approximately  $0.31 \times \pi/c$  away from the  $L$  valleys along the high symmetry line  $L-M$ , are 0.61 eV above  $E_0$ . Similar energies for the satellite valleys have been adopted by Albrecht *et al.* in their three-valley ( $\Gamma$ ,  $K$ , and  $U$ ) MC simulation of bulk wurtzite-phase AlN [31]. The upper  $L$  valleys are 0.92 eV above  $E_0$ . These satellite valley energies are much smaller than those of GaN, as compared in Table I. Use of the lowest five conduction bands permits simulations of carrier transport to kinetic energies as high as 8 eV. The calculated band gap is 4.35 eV, smaller than the approximately 6.0 eV reported from experimental measurements, which is also due to the underestimation of the band gaps for semiconductors with DFT calculations.

The electron effective masses in different valleys of the lowest conduction band are listed in Table III and compared with previous results [31,42,46,47,49]. For the first conduction band at the  $\Gamma$  point, the effective mass is close to an isotropic value of  $0.31 m_0$ , the same value used by Albrecht *et al.* [31]. Experimental measurements have estimated that the electron effective mass ranges from  $0.233 m_0$  to  $0.336 m_0$  [67]. The effective mass for the second conduction band at  $\Gamma$  is  $0.36 m_0$ .

The phonon dispersion is shown in Fig. 6(b). The LO energy at  $\Gamma$  is approximately 110 meV. Both the longitudinal and the transverse acoustic-phonon sound velocities are listed in Table II. All the parameters agree well with previous results [61,62]. The first-principles electron-phonon emission and absorption scattering rates for AlN are shown

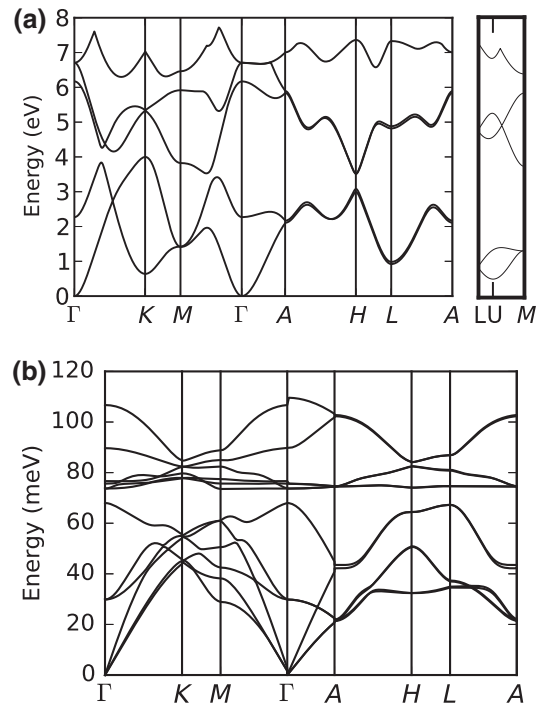


FIG. 6. (a) The energy dispersion of the first five conduction bands along several high-symmetry lines. The conduction band minimum at the  $\Gamma$  valley is set to zero. (b) Full phonon dispersion along several high-symmetry lines of wurtzite AlN.

in Fig. 7(a) both for polar and nonpolar scattering with optical phonons and in Fig. 7(b) both for polar and nonpolar scattering with acoustic phonons. Interestingly, the rate for polar scattering with acoustic phonons is the same order of magnitude as the rate for polar scattering with optical phonons for electrons with energies below 110 meV. Above 110 meV, the polar scattering with optical phonons is about ten times larger than the piezoelectric scattering.

The scattering rates calculated from the analytical formula are also plotted in Figs. 7(a) and 7(b). For the analytical rates of polar scattering with optical phonons, we use a static dielectric constant of 9.14 and a high-frequency dielectric constant of 4.84 [68]. For the analytical nonpolar scattering rates, we use a nonparabolicity factor of  $0.35 \text{ eV}^{-1}$ , a nonpolar acoustic deformation potential of 7.0 eV, and nonpolar optical deformation potential of  $1.32 \times 10^9 \text{ eV/cm}$ . We use a Gaussian smearing of 0.1 eV to deal with the energy conserving Dirac  $\delta$  functions.

The velocity-field and average carrier energy field characteristics of bulk AlN are shown in Fig. 5 and compared with those of GaN. An electron mobility of approximately  $450 \text{ cm}^2/(\text{V s})$  at RT is extracted from the low electric field region. Taniyasu *et al.* have measured a RT electron mobility of  $426 \text{ cm}^2/(\text{V s})$  for  $n$  type AlN with Si doping concentration of  $3 \times 10^{17} \text{ cm}^{-3}$  [69]. The peak drift velocity of AlN is smaller than that of GaN and the corresponding critical field is larger. This is due to the heavier



TABLE III. Electron effective mass (in unit of free electron mass  $m_0$ ) along different crystalline directions at different valleys of the first conduction band and acoustic phonons' sound velocities for AlN

	This work	Other work
$m_{\Gamma}^*$ ( $\Gamma \rightarrow K$ )	0.31	0.42 <sup>a</sup>
$m_K^*$ ( $K \rightarrow \Gamma$ )	0.64	0.54 <sup>b</sup> , 0.488 <sup>c</sup>
$m_K^*$ ( $K \rightarrow M$ )	0.65	0.54 <sup>b</sup>
$m_M^*$ ( $M \rightarrow K$ )	0.25	0.629 <sup>c</sup>
$m_M^*$ ( $M \rightarrow \Gamma$ )	1.20	
$m_{\Gamma}^*$ ( $\Gamma \rightarrow M$ )	0.31	0.40 <sup>a</sup> , 0.31 <sup>b</sup> , 0.26 <sup>c</sup> , 0.35 <sup>d</sup> , 0.25 <sup>e</sup> , 0.3433 <sup>f</sup>
$m_{\Gamma}^*$ ( $\Gamma \rightarrow A$ )	0.33	0.33 <sup>a</sup> , 0.35 <sup>d</sup> , 0.33 <sup>e</sup> , 0.2938 <sup>f</sup>
$m_A^*$ ( $A \rightarrow \Gamma$ )	-0.64	
$m_A^*$ ( $A \rightarrow H$ )	0.55	
$m_U^*$ ( $U \rightarrow L/M$ )	0.43	0.39 <sup>b</sup> , 0.495 <sup>c</sup>
$m_L^*$ ( $L \rightarrow H$ )	0.40	
$m_L^*$ ( $L \rightarrow A$ )	0.89	
$m_A^*$ ( $A \rightarrow L$ )	0.55	
$c_s^{LA}$ ( $\Gamma \rightarrow A$ )	10 877	
$c_s^{TA}$ ( $\Gamma \rightarrow A$ )	5880	

<sup>a</sup>Ref. [47].

<sup>b</sup>Ref. [31].

<sup>c</sup>Ref. [41].

<sup>d</sup>Ref. [49].

<sup>e</sup>Ref. [46].

<sup>f</sup>Ref. [42].

$\Gamma$  valley effective mass of AlN and also the smaller  $U$  valley minima. Albrecht *et al.* [31] have used a three-valley analytical band structure and ensemble MC technique to simulate the electron transport of wurtzite-phase AlN. A similar trend is observed for the electric field–drift velocity characteristics. However, a higher intrinsic low-field electron mobility of approximately  $850 \text{ cm}^2/(\text{V s})$  was reported since piezoelectric scattering was not included. We show in Fig. 8 the occupation of electrons at the first and the second conduction bands in reciprocal space at the field strength of  $800 \text{ kV/cm}$ . Particles populating the  $\Gamma$  valley exhibit the expected momentum shift along the electric field direction. The occupation of the satellite  $U$  and  $K$  valleys is larger in AlN than in GaN, a result of the smaller energy splitting from the conduction-band minimum. The  $L$  valley and the  $M$  valleys in the second conduction band are also occupied at large electric fields.

#### IV. SIMULATIONS OF AN $\text{Al}_{0.25}\text{Ga}_{0.75}\text{N}/\text{GaN}$ HEMT

In this section, we demonstrate the use of the first-principles electron transport properties in semiconductor device simulations by considering an  $\text{Al}_{0.25}\text{Ga}_{0.75}\text{N}/\text{GaN}$  HEMT. The device structure, shown in Fig. 9, is taken from Ref. [17], in which electrical stress test experiments

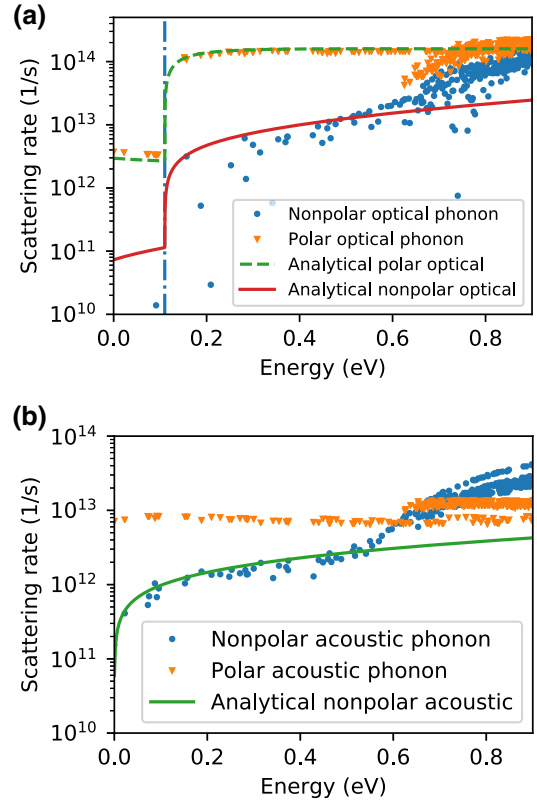


FIG. 7. (a) The calculated first-principles polar and nonpolar scattering with optical phonons. The vertical dot-dashed line is drawn at the energy of the highest-energy optical phonon mode and is plotted for eye guiding, serving as a separation between low and high energy carriers. (b) the calculated first-principles polar and nonpolar scattering with acoustic phonons in wurtzite AlN. A fine  $\mathbf{q}$  mesh of  $40 \times 40 \times 40$  and a Gaussian smearing of  $0.1 \text{ eV}$  are used in the calculations.

were performed on the HEMT. As the  $\text{Al}_{0.25}\text{Ga}_{0.75}\text{N}$  layer is not doped, the free electrons in the layer, mostly coming from energetic carriers in the GaN layer, are scarce and less energetic ( $<1 \text{ eV}$ ) after surpassing the interface barrier. These low-energy electrons locate likely around the  $\Gamma$  valley. Thus, the electron transport parameters of  $\text{Al}_{0.25}\text{Ga}_{0.75}\text{N}$  are approximated by interpolating the effective mass, deformation potentials, and the piezoelectric coefficient of AlN and GaN according to their respective compositions. The piezoelectric scattering rate is calculated analytically with the equation given in Ref. [70] as

$$\frac{1}{\tau} = \frac{m^* k_B T}{4\pi \hbar^3 k \rho} \left( \frac{e e_{pz}}{\epsilon_\infty v_s} \right)^2 \ln \left( 1 + \frac{4k^2}{q_D^2} \right), \quad (2)$$

where  $e_{pz}$  is a piezoelectric coefficient,  $k$  is the magnitude of the electron wavevector,  $\rho$  is the mass density of the material,  $\epsilon_\infty$  is the static dielectric constant,  $v_s$  is the sound velocity, and  $q_D$  is the Thomas-Fermi screening length. Fitting to the first-principles scattering rates, we obtain an  $e_{pz}$  of approximately  $1 \text{ C/m}^2$  for GaN and

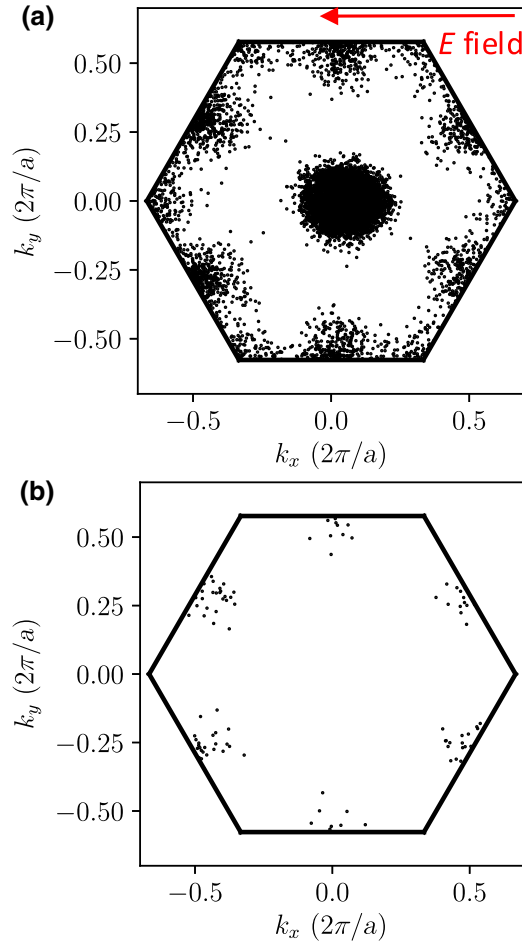


FIG. 8. For AlN, the distribution of MC particles on (a) the first conduction band and (b) the second conduction band in reciprocal space at an electric field strength of 800 kV/cm.

an  $e_{pz}$  of approximately  $1.3 \text{ C/m}^2$  for AlN. Note that for these fittings, we use the transverse acoustic phonon sound velocity for  $v_s$  as it results in larger scattering rates.

For the analytical selection of after-scattering final states, we assume the coupling constant proportional to  $1/(q^2 + q_D^2)$ , as assumed in Eq. (2). The coupling constant is a complex function of  $q$  and is anisotropic. Thus, it depends on the direction and polarization (pure dilation or shear along certain directions) of the phonons being emitted or absorbed. Different analytical forms of the coupling constants at small  $q$  have been given in the literature, based on different assumptions and approximations for the dominant phonons and the angular average over all phonon polarizations and directions [20,33,70,71]. However, the small  $q$  behavior of the coupling constant does not significantly affect electron transport, since scattering is almost elastic and small-angle collisions have little effect on transport. In the important range of large  $q$ , all the different forms assumed for the coupling constant yield a similar  $1/q^2$  dependence.

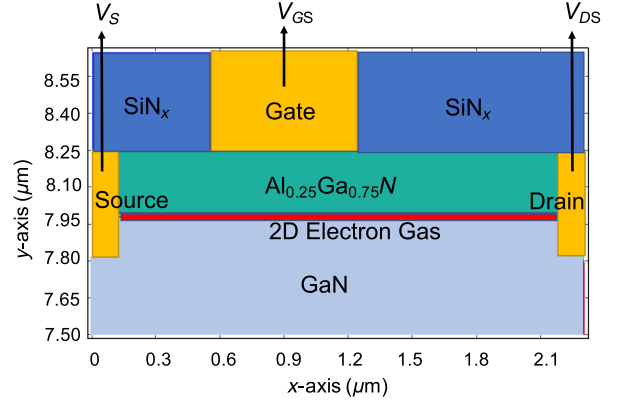


FIG. 9. Schematic diagram of an  $\text{Al}_{0.25}\text{Ga}_{0.75}\text{N}/\text{GaN}$  HEMT. Only the upper part of the device is shown. Different regions of the device are shown with different colors. The gate spans from 0.5 to 1.2  $\mu\text{m}$ . The 2D electron gas at the interface of  $\text{Al}_{0.25}\text{Ga}_{0.75}\text{N}$  and GaN is indicated in the red region.

With the assumed coupling constant proportional to  $1/(q^2 + q_D^2)$ , the probability distribution function for the momentum transferred,  $q$ , is

$$P(x) = \frac{\ln[(2+a)/(1-x+a)]}{\ln[(2+a)/a]}, \quad (3)$$

where  $a = q_D^2/2k^2$ ,  $x = \cos(\theta)$  and  $\theta$  is the scattering angle. The direct technique can then be used in MC simulations to determine the polar angle as  $x = 1 + a - a^r(a+2)^{1-r}$ , where  $r$  is a random number in  $[0,1]$ .

The Schottky barrier-height of  $n$  type GaN in contact with gold is 1.01 eV [72]. It is also known from Refs. [73,74] that the AlN/GaN valence band offset is 0.81 eV. Thus, for  $\text{Al}_{0.25}\text{Ga}_{0.75}\text{N}$  in contact with gold, we adopt the Schottky barrier height of 1.44 eV [75]. The bowing parameter  $b$  we adopt to calculate the band gap of the alloy and align the valence band edge and conduction band edge as  $E_g(\text{Al}_x\text{Ga}_{1-x}\text{N}) = (1-x) \cdot E_g(\text{GaN}) + x \cdot E_g(\text{AlN}) - b \cdot x \cdot (1-x)$  is 0.65 eV [76].

For  $\text{Al}_x\text{Ga}_{1-x}\text{N}/\text{GaN}$  HEMTs, both spontaneous polarization and piezoelectric polarization contribute to the formation of a 2DEG at the heterostructure interface without any doping in the channel. As III-V nitrides have significant piezoelectric coefficients [3,77], with the lattice-mismatch-caused strain and stress, the piezoelectric charge density at the  $\text{Al}_x\text{Ga}_{1-x}\text{N}/\text{GaN}$  HFET interface is estimated as  $5 \times 10^{13} \cdot x \text{ cm}^{-2}$ , where  $x$  is the aluminum mole fraction [3,6,77].

In these simulations of  $\text{Al}_{0.25}\text{Ga}_{0.75}\text{N}/\text{GaN}$  HEMTs, the device doping is taken from Ref. [17]. The piezoelectric charge density is  $1.25 \times 10^{13} \text{ cm}^{-2}$ , corresponding to an aluminum mole fraction of 0.25. With a mesh size of 1 nm at the interface, we set a  $\delta$  doping with a density of  $1.25 \times 10^{20} \text{ cm}^{-3}$  at the interface to mimic the piezoelectric polarization effect on the electrostatics of the

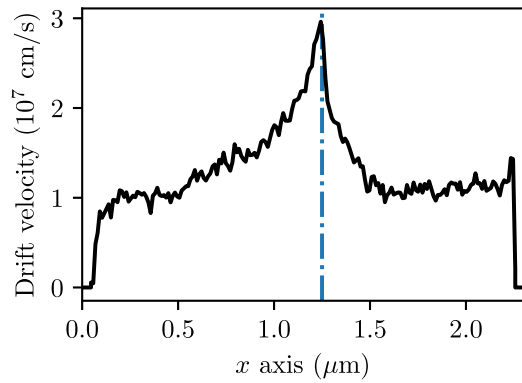


FIG. 10. The average drift velocity of electrons along the GaN channel for a thickness of 10 nm under the interface. The vertical dashed line indicates the gate edge at the drain end.

interface. For a prestress operating *on* condition (the gate-source (GS) bias  $V_{GS} = 0$  and the drain-source (DS) bias  $V_{DS} = 0.5$  V), we obtain a current density of 2.7 A/cm from our simulations, which agrees reasonably well with the experimentally measured current density of 2.26 A/cm [Ref. [17], Fig. 9(a)].

Here, we perform device simulations at a given bias condition ( $V_{GS} = 1$  V and  $V_{DS} = 10$  V) of the electrical stress tests to study the hot carrier transport that causes the threshold-voltage shift and transconductance degradation measured in Ref. [17]. The MC simulation lasts for about 9 ps with a time step of 0.05 fs. As MC simulations are intrinsically a transient calculation and performing a statistical average over the instantaneous quantities in equilibrium allows us to obtain the physical steady-state quantities. The average electron drift velocity in the GaN channel is shown in Fig. 10. This peak drift velocity of approximately  $3.0 \times 10^7$  cm/s at the gate-drain edge is larger than the steady-state peak drift velocity of  $2.5 \times 10^7$  cm/s shown in Fig. 3.

The average electron kinetic energy in the channel is shown in Fig. 11, as well as the lateral electric field in

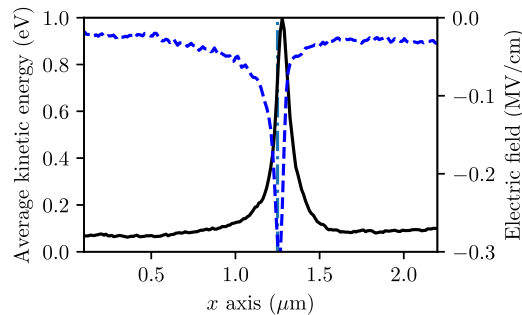


FIG. 11. The average kinetic energy of electrons (black solid line) and the lateral electric field (dashed blue line) along the GaN channel for a thickness of 10 nm under the interface. The vertical dashed line indicates the gate edge at the drain end.

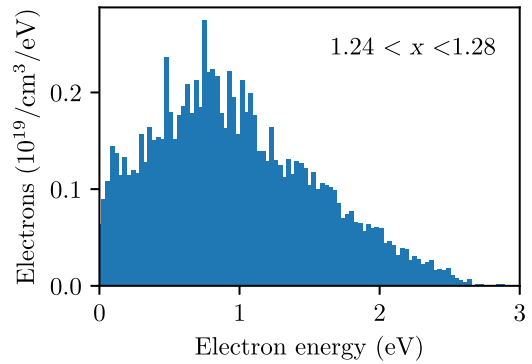


FIG. 12. A histogram showing the carrier energy distribution function at the gate-drain access region, from 1.24 to 1.28  $\mu\text{m}$ , and for a thickness of 10 nm under the interface. It is obtained through averaging the carrier energy distribution function at the same location in the time interval of 3–9 ps. The electron energy bin width is 0.03 eV.

the channel. Electrons are hottest at the gate-drain access region where the lateral electric field peaks. The average kinetic energy peak is close to 1.0 eV. The carrier energy distribution at the drain end of the GaN channel, where hot electrons are present, is shown in Fig. 12. Electrons with a kinetic energy around 1.0 eV are dominant in this region. Hot electrons can dehydrogenate point defects, as discussed in Refs. [78,79], and cause the observed device degradation. Quantitatively, the carrier energy distribution can be used to determine the hot-electron reaction rate with defects and thus the trap generation rate. Device degradation can then be simulated numerically [80]. This objective will be addressed in future work, together with developing an appropriate degradation model and comparing the simulation results with experimental device degradation data [17]. It is necessary to also include impact ionization because of the large applied bias and the presence of carriers with kinetic energies larger than the band gap of the channel material [11,26].

Braga *et al.* have shown that the electron quantization does not have a significant impact on the dc electrical characteristics, although the electron wave function can spread into the barrier and the substrate [75]. However, hot electrons affect the carrier transport when they travel into the bulk GaN and are captured by traps. Yamakawa *et al.* have also discussed that the overall current of the HEMTs is dominated by the polarization charge, so that including quantum corrections do not result in any significant difference [81].

## V. CONCLUSIONS

We show the electronic band structures, phonon dispersions, and electron-phonon scattering rates of both wurtzite GaN and AlN calculated using first-principles methods. The energies of valley minima are reported, as well as

their effective masses. In particular, we show that the *ab initio* calculations predict a piezoelectric scattering rate larger than previously assumed, even at RT. We also find that for electron collisions with the highest-energy optical phonon mode, nonpolar scattering by optical phonons contributes comparable to polar scattering. Nonpolar acoustic deformation potential and nonpolar optical deformation potential are reported for GaN and AlN.

The integration of *ab initio* methods into advanced semiconductor device simulations is demonstrated by studying high-field electron transport of bulk semiconductors and simulating high-electron-mobility transistors. By solving the Boltzmann transport equation with a synchronous ensemble MC technique and employing the first-principles electronic properties, we calculate the high-field transport characteristics of bulk GaN and bulk AlN and compare them with previously reported results. For AlN, inclusion of piezoelectric scattering results in a low-field electron mobility of approximately  $450 \text{ cm}^2/(\text{V s})$ , which is very close to the experimental value. We present simulation results for an  $\text{Al}_{0.25}\text{Ga}_{0.75}\text{N}/\text{GaN}$  HEMT, including electric field, average carrier kinetic energy, and drift velocity in the channel. The carrier energy distribution function in the conducting channel is presented, which is key to accurately determining hot-carrier-caused device degradation. Ways in which the simulation methods could be used to identify improved device designs are discussed. This predictive tool also provides an avenue to predict the electron transport properties of HEMTs based on other heterostructures, such as  $\text{Al}_x\text{In}_{1-x}\text{N}/\text{GaN}$ ,  $\gamma\text{-Al}_2\text{O}_3/\text{SrTiO}_3$ , and  $\text{Ga}_2\text{O}_3/(\text{Al}_x\text{Ga}_{1-x})_2\text{O}_3$ .

### ACKNOWLEDGMENTS

The authors gratefully acknowledge financial support from National Science Foundation Grant No. EECs-1508898, the US Army Research Laboratory through the Collaborative Research Alliance (CRA) Grant No. W911NF-12-2-0023 for Multi-Scale multidisciplinary Modeling of Electronic Materials (MSME), and the Air Force Office of Scientific Research through the HiREV program. Dr. Masahiko Matsubara is acknowledged for the help in building and running the EPW program in the group cluster at Boston University.

---

[1] J. B. Casady and R. W. Johnson, Status of silicon carbide (SiC) as a wide-bandgap semiconductor for high-temperature applications: A review, *Solid State Electron.* **39**, 1409 (1996).

[2] B. J. Baliga, Gallium nitride devices for power electronic applications, *Semicond. Sci. Technol.* **28**, 074011 (2013).

[3] P. M. Asbeck, E. T. Yu, S. S. Lau, G. J. Sullivan, J. VanHove, and J. Redwing, Piezoelectric charge densities in AlGaIn/GaN HFETs, *Electron. Lett.* **33**, 1230 (1997).

[4] M. A. Khan, D. T. Olson, J. M. Vanhove, and J. N. Kuznia, Vertical-cavity, room-temperature stimulated-emission from photopumped GaN films deposited over sapphire substrates using low-pressure metalorganic chemical vapor-deposition, *Appl. Phys. Lett.* **58**, 1515 (1991).

[5] J. J. Wierer, D. A. Steigerwald, M. R. Krames, J. J. O'Shea, M. J. Ludowise, G. Christenson, Y. C. Shen, C. Lowery, P. S. Martin, S. Subramanya, W. Gotz, N. F. Gardner, R. S. Kern, and S. A. Stockman, High-power AlGaInN flip-chip light-emitting diodes, *Appl. Phys. Lett.* **78**, 3379 (2001).

[6] O. Ambacher, J. Smart, J. R. Shealy, N. G. Weimann, K. Chu, M. Murphy, W. J. Schaff, L. F. Eastman, R. Dimitrov, L. Wittmer, M. Stutzmann, W. Rieger, and J. Hilsenbeck, Two-dimensional electron gases induced by spontaneous and piezoelectric polarization charges in N- and Ga-face AlGaIn/GaN heterostructures, *J. Appl. Phys.* **85**, 3222 (1999).

[7] A. Denisenko and E. Kohn, Diamond power devices. Concepts and limits, *Diam. Relat. Mater.* **14**, 491 (2005).

[8] M. Higashiwaki, K. Sasaki, A. Kuramata, T. Masui, and S. Yamakoshi, Development of gallium oxide power devices, *Phys. Status Solidi A* **211**, 21 (2014).

[9] T. Wang, W. Li, C. Ni, and A. Janotti, Band Gap and Band Offset of  $\text{Ga}_2\text{O}_3$  and  $(\text{Al}_x\text{Ga}_{1-x})_2\text{O}_3$  Alloys, *Phys. Rev. Appl.* **10**, 011003 (2018).

[10] M. Musolino, A. Tahraoui, L. Geelhaar, F. Sacconi, F. Panetta, C. De Santi, M. Meneghini, and E. Zanoni, Effect of Varying Three-Dimensional Strain on the Emission Properties of Light-Emitting Diodes Based on (In,Ga)N/GaN Nanowires, *Phys. Rev. Appl.* **7**, 044014 (2017).

[11] M. Moresco, F. Bertazzi, and E. Bellotti, Theory of high field carrier transport and impact ionization in wurtzite GaN. Part II: Application to avalanche photodetectors, *J. Appl. Phys.* **106**, 063719 (2009).

[12] J. B. Webb, H. Tang, J. A. Bardwell, and P. Coleridge, Growth of high mobility GaN and AlGaIn/GaN high electron mobility translator structures on 4h-SiC by ammonia molecular-beam epitaxy, *Appl. Phys. Lett.* **78**, 3845 (2001).

[13] L. Z. Wang, M. Yin, A. Khan, S. Muhtadi, F. Asif, E. S. Choi, and T. Datta, Scatterings and Quantum Effects in (Al, In)N/GaN Heterostructures for High-Power and High-Frequency Electronics, *Phys. Rev. Appl.* **9**, 024006 (2018).

[14] D. V. Christensen, Y. Frenkel, P. Schutz, F. Trier, S. Wissberg, R. Claessen, B. Kalisky, A. Smith, Y. Z. Chen, and N. Pryds, Electron Mobility in  $\gamma\text{-Al}_2\text{O}_3/\text{SrTiO}_3$ , *Phys. Rev. Appl.* **9**, 054004 (2018).

[15] D. Alden, J. S. Harris, Z. Bryan, J. N. Baker, P. Reddy, S. Mita, G. Callsen, A. Hoffmann, D. L. Irving, R. Collazo, and Z. Sitar, Point-Defect Nature of the Ultraviolet Absorption Band in AlN, *Phys. Rev. Appl.* **9**, 054036 (2018).

[16] I. C. Diallo and D. O. Demchenko, Native Point Defects in GaN: A Hybrid-Functional Study, *Phys. Rev. Appl.* **6**, 064002 (2016).

[17] R. Jiang, X. Shen, J. Fang, P. Wang, E. X. Zhang, J. Chen, D. M. Fleetwood, R. D. Schrimpf, S. W. Kaun, E. C. H. Kyle, J. S. Speck, and S. T. Pantelides, Multiple defects cause degradation after high field stress in AlGaIn/GaN HEMTs, *IEEE Trans. Device Mater. Reliab.* **18**, 364 (2018).

- [18] S. Mukherjee, Y. Puzyrev, J. Chen, D. M. Fleetwood, R. D. Schrimpf, and S. T. Pantelides, Hot-carrier degradation in GaN HEMTs due to substitutional iron and its complexes, *IEEE Trans. Electron Devices* **63**, 1486 (2016).
- [19] D. Bisi, M. Meneghini, M. Van Hove, D. Marcon, S. Stoffels, T. L. Wu, S. Decoutere, G. Meneghesso, and E. Zanoni, Trapping mechanisms in GaN-based MIS-HEMTs grown on silicon substrate, *Phys. Status Solidi A* **212**, 1122 (2015).
- [20] S. Vitinov, M. Nedjalkov, and V. Palankovski, A Monte Carlo model of piezoelectric scattering in GaN, *Numer. Methods Appl.* **4310**, 197 (2007).
- [21] J. Fang, W. G. Vandenberghe, B. Fu, and M. V. Fischetti, Pseudopotential-based electron quantum transport: Theoretical formulation and application to nanometer-scale silicon nanowire transistors, *J. Appl. Phys.* **119**, 035701 (2016).
- [22] J. Fang, S. Chen, W. G. Vandenberghe, and M. V. Fischetti, Theoretical study of ballistic transport in silicon nanowire and graphene nanoribbon field-effect transistors using empirical pseudopotentials, *IEEE Trans. Electron Devices* **64**, 2758 (2017).
- [23] M. V. Fischetti and S. E. Laux, Monte-Carlo analysis of electron-transport in small semiconductor-devices including band-structure and space-charge effects, *Phys. Rev. B* **38**, 9721 (1988).
- [24] H. Shichijo and K. Hess, Band-structure-dependent transport and impact ionization in GaAs, *Phys. Rev. B* **23**, 4197 (1981).
- [25] C. Jacoboni and L. Reggiani, The Monte-Carlo method for the solution of charge transport in semiconductors with applications to covalent materials, *Rev. Mod. Phys.* **55**, 645 (1983).
- [26] F. Bertazzi, M. Moresco, and E. Bellotti, Theory of high field carrier transport and impact ionization in wurtzite GaN. Part I: A full band Monte Carlo model, *J. Appl. Phys.* **106**, 063718 (2009).
- [27] C. Bulutay, B. K. Ridley, and N. A. Zakhleniuk, Full-band polar optical phonon scattering analysis and negative differential conductivity in wurtzite GaN, *Phys. Rev. B* **62**, 15754 (2000).
- [28] Y. R. Wu, M. Singh, and J. Singh, Sources of transconductance collapse in III-V nitrides - consequences of velocity-field relations and source/gate design, *IEEE Trans. Electron Devices* **52**, 1048 (2005).
- [29] J. M. Barker, R. Akis, D. K. Ferry, S. M. Goodnick, T. J. Thornton, D. D. Koleske, A. E. Wickenden, and R. L. Henry, High-field transport studies of GaN, *Physica B* **314**, 39 (2002).
- [30] U. V. Bhapkar and M. S. Shur, Monte Carlo calculation of velocity-field characteristics of wurtzite GaN, *J. Appl. Phys.* **82**, 1649 (1997).
- [31] J. D. Albrecht, R. P. Wang, P. P. Ruden, M. Farahmand, and K. F. Brennan, Monte Carlo calculation of electron transport properties of bulk AlN, *J. Appl. Phys.* **83**, 1446 (1998).
- [32] S. Yamakawa, S. Aboud, M. Saraniti, and S. M. Goodnick, Influence of the electron-phonon interaction on electron transport in wurtzite GaN, *Semicond. Sci. Technol.* **19**, S475 (2004).
- [33] S. Yamakawa, R. Akis, N. Faralli, M. Saraniti, and S. M. Goodnick, Rigid ion model of high field transport in GaN, *J. Phys.: Condens. Matter* **21**, 174206 (2009).
- [34] S. K. O'Leary, B. E. Foutz, M. S. Shur, U. V. Bhapkar, and L. F. Eastman, Monte Carlo simulation of electron transport in wurtzite aluminum nitride, *Solid State Commun.* **105**, 621 (1998).
- [35] Y. R. Wu, M. Singh, and J. Singh, Device scaling physics and channel velocities in AlGaIn/GaN HFETs: Velocities and effective gate length, *IEEE Trans. Electron Devices* **53**, 588 (2006).
- [36] P. D. Yoder, V. D. Natoli, and R. M. Martin, Ab-initio analysis of the electron-phonon interaction in silicon, *J. Appl. Phys.* **73**, 4378 (1993).
- [37] P. Giannozzi, *et al.*, Quantum espresso: A modular and open-source software project for quantum simulations of materials, *J. Phys.: Condens. Matter* **21**, 395502 (2009).
- [38] M. Schlipf and F. Gygi, Optimization algorithm for the generation of ONCV pseudopotentials, *Comput. Phys. Commun.* **196**, 36 (2015).
- [39] K. T. Delaney, P. Rinke, and C. G. Van de Walle, Auger recombination rates in nitrides from first principles, *Appl. Phys. Lett.* **94**, 191109 (2009).
- [40] A. Rubio, J. L. Corkill, M. L. Cohen, E. L. Shirley, and S. G. Louie, Quasi-particle band-structure of AlN and GaN, *Phys. Rev. B* **48**, 11810 (1993).
- [41] C. Bulutay, Electron initiated impact ionization in AlGaIn alloys, *Semicond. Sci. Technol.* **17**, L59 (2002).
- [42] M. Goano, E. Bellotti, E. Ghillino, G. Ghione, and K. F. Brennan, Band structure nonlocal pseudopotential calculation of the III-nitride wurtzite phase materials system. Part I. Binary compounds GaN, AlN, and InN, *J. Appl. Phys.* **88**, 6467 (2000).
- [43] M. Piccardo, L. Martinelli, J. Iveland, N. Young, S. P. DenBaars, S. Nakamura, J. S. Speck, C. Weisbuch, and J. Peretti, Determination of the first satellite valley energy in the conduction band of wurtzite GaN by near-band-gap photoemission spectroscopy, *Phys. Rev. B* **89**, 235124 (2014).
- [44] S. Marcinkevicius, T. K. Uzdavinyis, H. M. Foronda, D. A. Cohen, C. Weisbuch, and J. S. Speck, Intervalley energy of GaN conduction band measured by femtosecond pump-probe spectroscopy, *Phys. Rev. B* **94**, 235205 (2016).
- [45] C. K. Sun, Y. L. Huang, S. Keller, U. K. Mishra, and S. P. DenBaars, Ultrafast electron dynamics study of GaN, *Phys. Rev. B* **59**, 13535 (1999).
- [46] M. Suzuki and T. Uenoyama, Strain effect on electronic and optical properties of GaN/AlGaIn quantum-well lasers, *J. Appl. Phys.* **80**, 6868 (1996).
- [47] Y. N. Xu and W. Y. Ching, Electronic, optical, and structural-properties of some wurtzite crystals, *Phys. Rev. B* **48**, 4335 (1993).
- [48] M. Drechsler, D. M. Hofmann, B. K. Meyer, T. Detchprohm, H. Amano, and I. Akasaki, Determination of the conduction-band electron effective-mass in hexagonal GaN, *Jpn. J. Appl. Phys.* **34**, L1178 (1995).
- [49] K. Kim, W. R. L. Lambrecht, B. Segall, and M. vanSchilf-gaarde, Effective masses and valence-band splittings in GaN and AlN, *Phys. Rev. B* **56**, 7363 (1997).
- [50] S. L. Wang, Y. L. Dou, H. X. Liu, Z. Y. Lin, and H. L. Zhang, Electron momentum and energy relaxation times

- in wurtzite GaN, InN and AlN: A Monte Carlo study, *J. Electron. Mater.* **47**, 1560 (2018).
- [51] C. Verdi and F. Giustino, Frohlich Electron-Phonon Vertex from First Principles, *Phys. Rev. Lett.* **115**, 176401 (2015).
- [52] S. Ponce, E. R. Margine, C. Verdi, and F. Giustino, EPW: Electron-phonon coupling, transport and superconducting properties using maximally localized wannier functions, *Comput. Phys. Commun.* **209**, 116 (2016).
- [53] F. Giustino, M. L. Cohen, and S. G. Louie, Electron-phonon interaction using Wannier functions, *Phys. Rev. B* **76**, 165108 (2007).
- [54] A. A. Mostofi, J. R. Yates, Y. S. Lee, I. Souza, D. Vanderbilt, and N. Marzari, Wannier90: A tool for obtaining maximally-localised Wannier functions, *Comput. Phys. Commun.* **178**, 685 (2008).
- [55] S. Ponce, E. R. Margine, and F. Giustino, Towards predictive many-body calculations of phonon-limited carrier mobilities in semiconductors, *Phys. Rev. B* **97**, 121201(R) (2018).
- [56] O. Lagerstedt and B. Monemar, Variation of lattice-parameters in GaN with stoichiometry and doping, *Phys. Rev. B* **19**, 3064 (1979).
- [57] V. Litovchenko, A. Grygoriev, A. Evtukh, O. Yilmazoglu, H. Hartnagel, and D. Pavlidis, in 10th IEEE International Vacuum Electronics Conference, IEEE, Angelicum Univ, Rome, Italy (2009), pp. 271.
- [58] F. Bertazzi, M. Goano, X. Y. Zhou, M. Calciati, G. Ghione, M. Matsubara, and E. Bellotti, Looking for Auger signatures in III-nitride light emitters: A full-band Monte Carlo perspective, *Appl. Phys. Lett.* **106**, 061112 (2015).
- [59] A. M. Witowski, K. Pakula, J. M. Baranowski, M. L. Sadowski, and P. Wyder, Electron effective mass in hexagonal GaN, *Appl. Phys. Lett.* **75**, 4154 (1999).
- [60] S. Chen and G. Wang, High-field properties of carrier transport in bulk wurtzite GaN: A Monte Carlo perspective, *J. Appl. Phys.* **103**, 023703 (2008).
- [61] V. Y. Davydov, Y. E. Kitaev, I. N. Goncharuk, A. N. Smirnov, J. Graul, O. Semchinova, D. Uffmann, M. B. Smirnov, A. P. Mirgorodsky, and R. A. Evarestov, Phonon dispersion and Raman scattering in hexagonal GaN and AlN, *Phys. Rev. B* **58**, 12899 (1998).
- [62] C. Bungaro, K. Rapcewicz, and J. Bernholc, Ab initio phonon dispersions of wurtzite AlN, GaN, and InN, *Phys. Rev. B* **61**, 6720 (2000).
- [63] K. Sarasamak, S. Limpijumnong, and W. R. L. Lambrecht, Pressure-dependent elastic constants and sound velocities of wurtzite SiC, GaN, InN, ZnO, and CdSe, and their relation to the high-pressure phase transition: A first-principles study, *Phys. Rev. B* **82**, 035201 (2010).
- [64] H. Frohlich, Electrons in lattice fields, *Adv. Phys.* **3**, 325 (1954).
- [65] M. E. Levinshtein, S. L. Rumyantsev, and M. S. Shur, *Properties of Advanced Semiconductor Materials: GaN, AlN, InN, BN, SiC, SiGe* (John Wiley & Sons, New York, 2001).
- [66] B. C. Lee, K. W. Kim, M. Dutta, and M. A. Stroschio, Electron-optical-phonon scattering in wurtzite crystals, *Phys. Rev. B* **56**, 997 (1997).
- [67] E. Silveira, J. A. Freitas, O. J. Glembocki, G. A. Slack, and L. J. Schowalter, Excitonic structure of bulk AlN from optical reflectivity and cathodoluminescence measurements, *Phys. Rev. B* **71**, 041201(R) (2005).
- [68] A. T. Collins, E. C. Lightowers, and P. J. Dean, Lattice vibration spectra of aluminum nitride, *Phys. Rev.* **158**, 833 (1967).
- [69] Y. Taniyasu, M. Kasu, and T. Makimoto, Increased electron mobility in n-type si-doped AlN by reducing dislocation density, *Appl. Phys. Lett.* **89**, 182112 (2006).
- [70] D. Vasileska, "Scattering mechanisms," [nanoHUB.org](http://nanoHUB.org).
- [71] B. K. Ridley, *Quantum Processes in Semiconductors* (Oxford University Press, Oxford, 2013).
- [72] M. R. H. Khan, T. Detchprohm, P. Hacke, K. Hiramatsu, and N. Sawaki, The barrier height and interface effect of a Au-n-GaN Schottky diode, *J. Phys. D: Appl. Phys.* **28**, 1169 (1995).
- [73] S. H. Wei and A. Zunger, Valence band splittings and band offsets of AlN, GaN, and InN, *Appl. Phys. Lett.* **69**, 2719 (1996).
- [74] G. Martin, A. Botchkarev, A. Rockett, and H. Morkoc, Valence-band discontinuities of wurtzite GNN, AlN, and InN heterojunctions measured by X-ray photoemission spectroscopy, *Appl. Phys. Lett.* **68**, 2541 (1996).
- [75] N. Braga, R. Mickevicius, R. Gaska, X. Hu, M. S. Shur, M. A. Khan, G. Simin, and J. Yang, Simulation of hot electron and quantum effects in AlGaIn/GaN heterostructure field effect transistors, *J. Appl. Phys.* **95**, 6409 (2004).
- [76] S. R. Lee, A. F. Wright, M. H. Crawford, G. A. Petersen, J. Han, and R. M. Biefeld, The band-gap bowing of  $\text{Al}_x\text{Ga}_{1-x}\text{N}$  alloys, *Appl. Phys. Lett.* **74**, 3344 (1999).
- [77] A. Bykhovski, B. Gelmont, and M. Shur, The influence of the strain-induced electric-field on the charge-distribution in GaN-AlN-GaN structure, *J. Appl. Phys.* **74**, 6734 (1993).
- [78] Y. S. Puzyrev, T. Roy, M. Beck, B. R. Tuttle, R. D. Schrimpf, D. M. Fleetwood, and S. T. Pantelides, Dehydrogenation of defects and hot-electron degradation in GaN high-electron-mobility transistors, *J. Appl. Phys.* **109**, 034501 (2011).
- [79] Y. Puzyrev, S. Mukherjee, J. Chen, T. Roy, M. Silvestri, R. D. Schrimpf, D. M. Fleetwood, J. Singh, J. M. Hinckley, A. Paccagnella, and S. T. Pantelides, Gate bias dependence of defect-mediated hot-carrier degradation in GaN HEMTs, *IEEE Trans. Electron Devices* **61**, 1316 (2014).
- [80] I. Starkov, S. Tyaginov, H. Enichlmair, J. Cervenka, C. Jungemann, S. Carniello, J. M. Park, H. Ceric, and T. Grasser, Hot-carrier degradation caused interface state profile-simulation versus experiment, *J. Vac. Sci. Technol. B* **29**, 01AB09 (2011).
- [81] S. Yamakawa, S. Goodnick, S. Aboud, and M. Saraniti, Quantum corrected full-band cellular Monte Carlo simulation of AlGaIn/GaN HEMTs, *J. Comput. Electron.* **3**, 299 (2004).